Li-Ion Cell Operation at Low Temperatures

Yan Ji, Yancheng Zhang and Chao-Yang Wang

J. Electrochem. Soc. 2013, Volume 160, Issue 4, Pages A636-A649.
doi: 10.1149/2.047304jes

Journal of The Electrochemical Society, **160** (4) A636-A649 (2013)
0013-4651/2013/160(4)/A636/14/$31.00 © The Electrochemical Society

Li-Ion Cell Operation at Low Temperatures

Yan Ji,[*] Yancheng Zhang,[**] and Chao-Yang Wang[,z]**

Electrochemical Engine Center (ECEC) and Department of Mechanical and Nuclear Engineering, The Pennsylvania State University, University Park, Pennsylvania 16802, USA

Substantially reduced energy and power capabilities of lithium-ion cell operating at low temperatures pose a technical barrier for market penetration of hybrid electric vehicles and pure electric vehicles. The present work delineates Li-ion cell behaviors at low temperatures by a combined experimental and modeling approach. An electrochemical-thermal coupled model, incorporating concentration- and temperature-dependent transport and kinetic properties, is applied and validated against 2.2Ah 18650 cylindrical cells over a wide range of temperatures (−20°C to 45°C) and discharge rates. Simulation and experimental results demonstrate the dramatic effects of cell self-heating upon electrochemical performance. A nonisothermal Ragone plot accounting for these important thermal effects is proposed for the first time for Li-ion cells and more generally for thermally coupled batteries. Detailed resistance analysis indicates that performance limits at −20°C depend on not only discharge rates but also thermal conditions. Optimization of cell design parameters and material properties is performed for 1 C rate discharge starting from −20°C, where the principal performance limitations are found to be Li^+ diffusion in the electrolyte and solid-state Li diffusion in graphite particles, instead of charge-transfer kinetic or ohmic resistance.
 [DOI: 10.1149/2.047304jes]

Manuscript submitted December 18, 2012; revised manuscript received January 22, 2013. Published February 13, 2013.

Increases in gasoline price and greenhouse gas emissions have spurred the growth of hybrid electric vehicles (HEV) and pure electric vehicles (EVs). Rechargeable Li-ion batteries are the leading candidate for these vehicles due to their high energy and power density relative to other battery chemistries. A large market penetration of HEVs and EVs requires overcoming a series of technical barriers for Li-ion batteries. One issue is significantly reduced energy and power densities at low temperatures.[1] For plug-in HEVs, batteries are required to function under unassisted operation, charge at −30°C, and survive at −46°C. For power assist HEVs, batteries should be able to deliver 5 kW cold-cranking power (three 2-s pulses, 10-s rests between) at −30°C.[2]

Much work has been conducted to improve performance and understand the rate-limiting factors of Li-ion batteries at low temperatures. Due to the high freezing points of widely used carbonate-based solvents (EC, DMC), a prevalent area of research is to seek electrolytes with lower freezing point and higher conductivity. With the use of solvent blends, co-solvent, novel electrolyte salts and electrolyte additives, the Li-ion cells are able to survive and even show good performance down to −60°C.[3–8] At the same time, electrochemical techniques are employed to examine cell resistances. Electrochemical impedance spectroscopy (EIS) is popular because of its ability to separate cell impedances according to their rate constants.[9–13] Analysis of EIS data shows the dominance of charge-transfer resistance at subzero temperature, due to its high activation energy.[14–16] In addition, investigations on graphite anode found considerable loss of lithiation capacity below −20°C. Cell limitations might also arise from the substantially lowered Li diffusivity in the graphite active material.[17–22]

It is generally believed that the poor performance of Li-ion cells at low temperatures are associated with: poor electrolyte conductivity, sluggish kinetics of charge transfer, increased resistance of solid electrolyte interphase (SEI), and slow Li diffusion through the surface layers and through the bulk of active material particles. Based on this understanding, extensive work is carried out to boost performance generally in two ways: (1) to modify interfacial property to reduce the high activation energy of charge-transfer kinetics and SEI resistance, by surface coating[23–25] or changing electrolyte composition;[3,6,8,26,27] and (2) to increase interfacial area by using nanostructured electrodes or different electrode morphology.[14,15,28,29]

Until now, investigations of low-temperature behaviors of Li-ion cells have been limited to experimental measurements and observations. A basic understanding of cell behavior is absent, due to the inherent limitations of available experimental techniques. For instance, the prevailing electrochemical techniques include electrochemical impedance spectroscopy (EIS), direct current (DC) polarization and cyclic voltammetry (CV). All of these measurements are conducted in the vicinity of equilibrium states, where large concentration polarizations in the electrolyte and solid particles have not been established. In contrast, large concentration polarizations exist during cell operation at high rates or low temperatures. These polarizations would induce very different cell behaviors, when electrochemical processes are coupled with the concentration dependence of equilibrium potential, ionic conductivity, salt diffusivity and solid state diffusivity.

Moreover, Li-ion cell operation at low temperatures is inherently linked to thermal effects, where internal heat generation is significant due to greatly increased cell resistance and very strong dependency of kinetic and transport properties on temperature in the subzero range. For instance, a tenfold increase in resistance relative to room temperature has been measured in commercial cells at −20°C.[13] Such interactions between electrochemical and thermal dynamics in Li-ion cells have not heretofore been explored in the literature.

In tandem with experimental studies, fundamental modeling based on concentrated solution theory and the technique of volume averaging for porous electrodes was pioneered by Newman and his co-workers[30–32] in early 1990s and widely used in the subsequent literature. In 2000 Gu and Wang[33] proposed an electrochemical-thermal (ECT) fully coupled framework able to simultaneously predict battery electrochemical and thermal behaviors. Song and Evans[34] also attempted the modeling of lithium polymer batteries by solving electrochemical and thermal equations simultaneously, although only electrolyte conductivity and salt diffusivity are considered as functions of temperature. In 2003 Srinivasan and Wang[35] incorporated all relevant kinetic and transport properties as dependences on temperature, as well as the state of charge (SOC) dependence of entropic heat. In 2008 Kumaresan et al.[36] updated the temperature and concentration dependence of electrolyte properties obtained from recent experimental data. However, the model is validated only at low discharge rates (no larger than 1 C) from 15°C to 45°C, where electrochemical-thermal coupling is insignificant. Recently, due to the revived interest in large-format batteries, their modules and packs for electric and hybrid vehicles, ECT modeling of Li-ion batteries in multi-dimensions was exercised by Gerver et al.,[37] Kim et al.,[38] and Luo and Wang.[39]

Despite the decade-long progress in ECT models,[34–46] no modeling study of Li-ion performance at subzero temperatures has been attempted. In particular, there has been no exploration of cell performance in the presence of remarkable temperature rise that naturally occurs in Li-ion cell usage at low temperatures. The overriding objective of the present work is to explore the basic nature of Li-ion cell operation at low temperatures, both experimentally and numerically.

[*]Electrochemical Society Student Member.
[**]Electrochemical Society Active Member.
[z]E-mail: cxw31@psu.edu

Table I. Design Parameters of 18650 test cell.

Parameters	Anode (Graphite)	Separator	Cathode (NCM)
Thickness (μm)	81	20	78
Porosity	0.264	0.46	0.281
Loading (mAh/cm^2)	4.5	—	3.9
Electrolyte concentration (mol/L)		1.2	
Particle (agglomerate) radius (μm)	10	—	5

Experimental

To explore the strong interplay between electrochemical and thermal dynamics, 18650 cylindrical cells of 2.2Ah are used in the present study. These cells consist of $LiNi_{1/3}Mn_{1/3}Co_{1/3}O_2$ (NCM) cathode and graphite anode, have a nominal capacity of 2.2Ah, ~600 cm^2 electrode area and 50 cm coating length, and weigh 44g. A list of design parameters for the test cells is given in Table I. Details of cell fabrication have been extensively described in the literature, e.g. in the authors' own work,[47] and thus are not repeated here.

Battery charge is performed at room temperature by a constant current (0.7 C) followed by constant voltage (4.2V) protocol with 1/20 C cutoff current. The cutoff voltage for discharge is 2.5V. A Tenney Environmental Chamber (with Watlow Series 942 Controller) is used to provide constant temperature environment for all the tests. Thermocouples are used to measure the cell surface temperature, located midway along the length of the 18650 cells. In order for the cell to reach thermal equilibrium before each charge or discharge operation, cells are kept for 4 h rest at each temperature except at 25°C, where 1 h rest is used.

Electrochemical-Thermal (ECT) Coupled Model

Applying the fully coupled electrochemical-thermal model of Gu and Wang,[33] the following conservation equations are solved:

Charge conservation in solid electrodes:

$$\nabla \cdot \left(\sigma_s^{eff} \nabla \phi_s\right) - j = 0 \quad [1]$$

Charge conservation in electrolyte:

$$\nabla \cdot \left(\kappa^{eff} \nabla \phi_e + \kappa_D^{eff} \nabla \ln c_e\right) + j = 0 \quad [2]$$

in which the effective diffusional ionic conductivity:

$$\kappa_D^{eff} = \frac{2RT\kappa^{eff}}{F}\left(t^+ - 1\right)\left(1 + \frac{d \ln f_\pm}{d \ln c_e}\right) \quad [3]$$

Material conservation in electrolyte:

$$\varepsilon \frac{\partial c_e}{\partial t} = \nabla \cdot \left(D_e^{eff} \nabla c_e\right) + \frac{1 - t_+}{F} j \quad [4]$$

Material conservation in solid particles:

$$\frac{\partial c_s}{\partial t} = \frac{1}{r^2}\frac{\partial}{\partial r}\left(D_s r^2 \frac{\partial c_s}{\partial r}\right) \quad [5]$$

with boundary condition on particle surface:

$$-D_{s,i}\left.\frac{\partial c_{s,i}}{\partial r}\right|_{r=R_i} = \frac{i}{F} \quad [6]$$

Butler-Volmer equation for charge transfer kinetics:

$$i = i_0\left[\exp\left(\frac{\alpha_a F}{RT}\eta\right) - \exp\left(-\frac{\alpha_c F}{RT}\eta\right)\right] \quad [7]$$

in which the kinetic overpotential:

$$\eta = \phi_s - \phi_e - U_i(c_{s,i}) - iR_f \quad [8]$$

and exchange current density:

$$i_0 = k(T)\, c_{s,i}^{\alpha_c} c_e^{\alpha_a} (c_{s,\max} - c_{s,i})^{\alpha_a} \quad [9]$$

Mapping between reaction current density on particle surface and volumetric current density in the electrodes:

$$j = ai \quad [10]$$

Energy conservation of the whole cell (lumped thermal model):

$$mc_p \frac{dT}{dt} = \dot{Q} + hA_s(T_\infty - T) \quad [11]$$

where h is the convective heat transfer coefficient, A_s the cell surface area, $hA_s(T_\infty - T)$ is the convective heat. The heat generation power:

$$\dot{Q} = A_e \int_0^L j(\phi_s - \phi_e - U) + j\left(T\frac{dU}{dT}\right) + \sigma_s^{eff}\nabla\phi_s \cdot \nabla\phi_s + \kappa^{eff}\nabla\phi_e \cdot \nabla\phi_e + \kappa_D^{eff}\nabla \ln c_e \cdot \nabla\phi_e \, dx \quad [12]$$

in which L is the sum of the anode, separator and cathode thicknesses, A_e is the electrode area, $j(\phi_s - \phi_e - U)$ represents kinetic heat, $j(T\frac{dU}{dT})$ is the reversible heat, $\sigma_s^{eff}\nabla\phi_s \cdot \nabla\phi_s$, $\kappa^{eff}\nabla\phi_e \cdot \nabla\phi_e$ and $\kappa_D^{eff}\nabla \ln c_e \cdot \nabla\phi_e$ are joule heat from electronic resistance, ionic resistance and concentration overpotential respectively.

This ECT model is supplemented by the list of cell design parameters given in Table I, and the electrochemical and material properties described in Appendix B as well as in Table II. In addition, thermal parameters also required by the ECT model are estimated below. Numerical solutions of the present model over a very wide range of operating conditions, cell designs, and material properties, as presented in the following, are made possible by robust algorithms

Table II. Electrochemical Properties.

Properties	Graphite (Li_xC_6)	$Li_yNi_{1/3}Mn_{1/3}Co_{1/3}O_2$
Exchange current density i_0 (A/m^2)	12[35] ($x = 0.5$)	2[b] ($y = 0.5$)
Activation energy of i_0 (kJ/mol)	68[16]	50[16]
Charge transfer coefficient α_a α_c	0.5 0.5[a]	0.5 0.5[a]
Film resistance R_f (Ω cm^2)	10[b]	10[b]
Activation energy of R_f (kJ/mol)	50[b]	50[b]
Solid state diffusivity D_s (m^2/s)	$1.6 \times 10^{-14}(1.5 - x)^{1.5}$[45]	3×10^{-14}[45, 57]
Activation energy of D_s (kJ/mol)	30[58]	30[a]
Contact resistance (Ω cm^2)	6[b]	

[a]assumed values
[b]extracted from model-experimental comparison

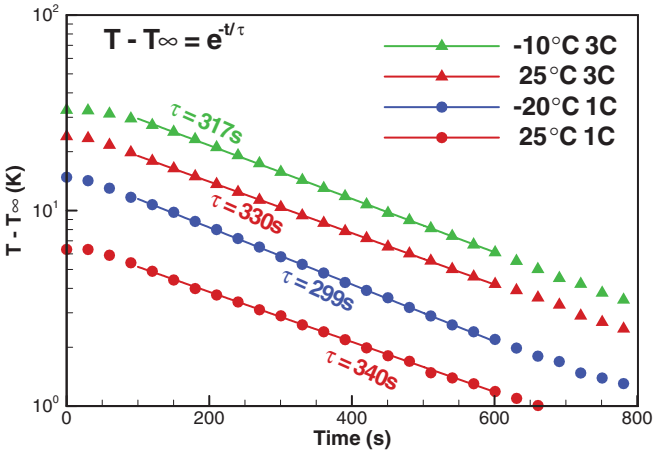

Figure 1. Cell temperature evolution after current interruption for estimation of surface heat transfer coefficient.

offered in AutoLion, a commercial software package for analyses of electrochemical and thermal interactions of Li-ion batteries and systems.

Estimation of thermal parameters.— In the present work, we apply a lumped thermal model, assuming spatially uniform temperature within the 18650 cell. Consequently, we eliminate the need for thermal conductivity in the cell; however, the heat capacity and heat transfer coefficient between the cell and ambient are still needed in the energy balance equation. An extensive literature survey found that the heat capacity of 18650 cells falls in the range of 800 ∼ 1000J/(KgK);[48,49] thus the value of 823J/(KgK)[49] is selected in the present study.

The external heat transfer coefficient, indicative of the cell cooling capability, can be measured by monitoring the cell temperature evolution after interruption of the discharge current at cutoff voltage. The heat of mixing during the relaxation process is small if the transport properties are sufficiently high.[43] To minimize the effect of heat mixing, cell data at room temperature and low C rates is preferred. Cell data at other conditions are also collected to see their applicability. The energy balance during the relaxation is written as:

$$mc_p \frac{dT}{dt} = hA_s(T_\infty - T) \qquad [13]$$

in which h is the convective heat transfer coefficient, A_s the cell surface area, m the cell mass, and c_p the specific heat. The solution to this equation has a simple exponential form:

$$T - T_\infty = e^{-t/\tau} \qquad [14]$$

where the characteristic cooling time $\tau = mc_p/hA_s$.

The temperature evolutions after the interruption of current have been analyzed using equation 14, as shown in Figure 1. The temperature data are sampled at the end of 25°C (1 C, 3 C) discharge, −10°C (3 C) discharge and −20°C (1 C) discharge respectively. The data from these four cases show a trend of straight lines in the logarithm plot, except for a few points at the beginning of the cooling process. Here, a much gentler decrease of temperature (especially after the low temperature high rate discharge) is seen probably owing to the heat of mixing. Using the least-squares algorithm, curve fittings are performed in the time range of 100s ∼ 600s to avoid the mixing effect at the beginning and larger error due to smaller temperature difference at later times. As shown in Figure 1, the characteristic cooling times τ for the four cases are very close to each other. The average τ value of 322s has been used as the initial guess to fit experimental data. It is found later that τ = 312s offers the best fitting result. The corresponding heat transfer coefficient is 28.4W/(m^{2}K), as calculated by the given value of cell specific heat, mass and dimensions.

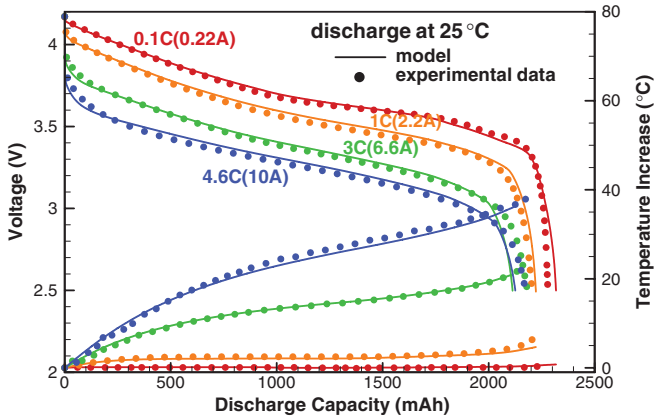

Figure 2. Validation A: C-rate effect for cell discharge from 25°C.

Model Validation

Model validation in the present work covers a wide range of C-rates and ambient temperatures, divided into three subgroups: (A) C-rate effect at room temperature, (B) temperature effect at a moderate discharge rate, and (C) C-rate effect from a subzero temperature. To fully delineate electrochemical performance that is strongly coupled with thermal behaviors in low-temperature operation, both voltage and temperature curves are compared between model predictions and experimental data.

Validation group A involves cells discharged at 0.1 C, 1 C, 3 C and 4.6 C rates, starting from 25°C. Cell voltage and temperature as a function of discharge capacity (or state of charge, SOC) are plotted in Figure 2, showing excellent agreement between model predictions and experimental data in both voltage and temperature evolutions. As expected, the cell temperature rise is more significant at higher discharge rate, due to a larger amount of heat generated from increased voltage loss. The cell discharge capacity, however, reduces minimally even at 4.6 C rate, owing to the increased temperature that enhances electrochemical kinetics and mass transport.

Validation B is intended to assess the temperature effect, where cells are discharged at 1 C rate but start with different temperatures: 45°C, 25°C, 0°C, −10°C and −20°C, as shown in Figure 3. The agreement between model and experiment is also good, except for a slight over-prediction on voltage near the cutoff voltage for 0°C and −10°C cases. Both cell voltage and capacity are lowered with the decrease

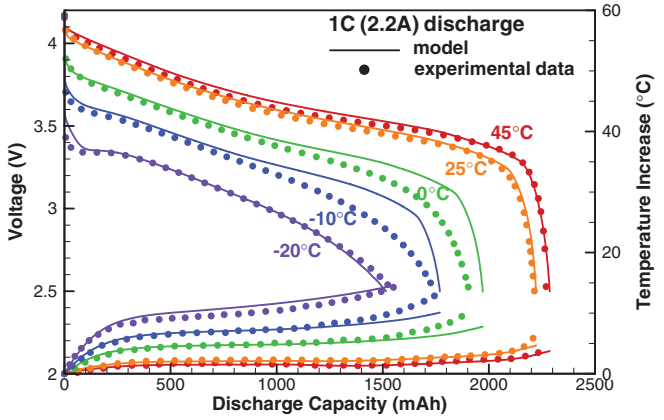

Figure 3. Validation B: Discharge with 1 C rate starting from various temperatures.

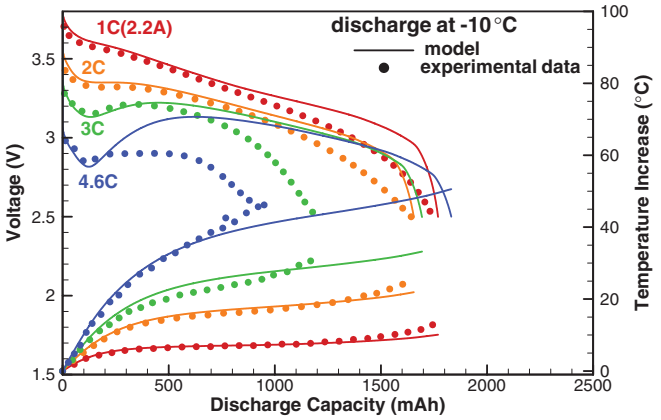

Figure 4. Validation C: C-rate effect for cell discharge from −10°C.

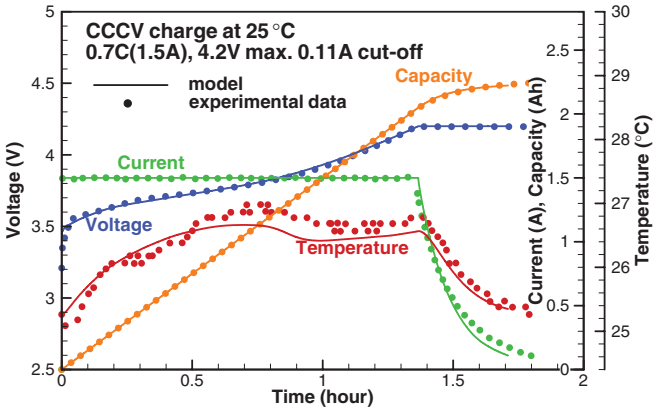

Figure 5. Validation of CC-CV charge at 25°C.

of temperature, especially at subzero temperatures. Accordingly, cell temperature rise is more marked at a lower ambient temperature due to higher cell resistance and larger voltage loss.

Validation C is used to study the rate effect at subzero temperatures. −10°C is selected as the ambient temperature since it is representative of a subzero temperature in automotive applications and at the same time is still capable of delivering reasonably high rate performance. The cell is subjected to discharge at 1 C, 2 C, 3 C and 4.6 C rates, as shown in Figure 4. Model predictions match well with experimental data at 1 C and 2 C rates, despite a little voltage over prediction near cutoff voltage. At 3 C rate, the deviation in cell voltage develops after 500 mAh discharge capacity. Experimental data shows more rapid voltage decay after rebound to 3.22 V, resulting in 1/3 lower cell capacity than model prediction. At 4.6 C rate, the discrepancy in cell voltage starts earlier, at ∼250 mAh discharge capacity, where a mild voltage rebound is observed experimentally. After that, the predicted cell voltage rebounds more significantly than the experimental data, leading to large deviation in discharge capacity. Both 3 C and 4.6 C cases show strong interaction of cell electrochemical and thermal dynamics, as demonstrated by voltage recovery and marked temperature rise in low-temperature operation.

We hypothesize that the large discrepancy between the predicted and measured voltage curves shown in Figure 4 is caused by extremely high sensitivity of cell performance at sub-freezing temperatures to operating conditions, cell design parameters, and material properties, as to be shown later. Because of such high sensitivity, any spatially non-uniform temperature field existing in a 18650 cylindrical cell may dramatically impact the cell's discharge characteristics. Work is underway to explore this hypothesis by setting up a three-dimensional model with full electrochemical and thermal coupling and results will appear in a future publication.

In addition to cell discharge behaviors, validation is also performed during charge operation. Cells are charged at 25°C with the CC-CV protocol described in the experimental section. A comparison between the model predictions and experimental data is also made for this charge process, as shown in Figure 5. Good agreement is seen in cell voltage, current, capacity, and temperature. Over 90% SOC is completed during the CC period, which takes about 78% of the total charge time, indicating good charge performance. Despite small temperature rise in this case, good agreement is seen for the temperature curve, implying reliable material properties used, such as electrolyte conductivity and reversible entropic heat, which are dominant factors during low-rate charge.

In summary, the present ECT model provides good prediction for rate effects at room temperature (4.6 C or higher), and temperature effects (ranging from −20°C to 45°C) at moderate rates (1 C ∼ 2 C). For very high-rate operation at very low temperatures, there still exists discrepancy between model and experiment, which is a research topic currently under investigation.

Analysis of Low-Temperature Characteristics

In this section, we use the experimentally validated ECT model to explore low-temperature cell behaviors, specifically in terms of voltage loss and heat generation.

One can divide the cell voltage loss into those due to: (1) electrical resistance in electrodes ΔV_s, (2) charge transfer kinetics on the active material-electrolyte interface ΔV_k, (3) ionic resistance and concentration polarization in electrolyte ΔV_e, (4) concentration polarization inside active material particles ΔV_p, as well as (5) electrical resistance from the imperfect contact of electrodes, current collectors and tabs ΔV_c. Mathematical definitions of these individual voltage losses are given in Appendix A. In according with these voltage losses, each area-specific resistance is defined by dividing the voltage drop by the operational current:

$$R_i = \frac{\Delta V_i}{I} A_e \qquad [15]$$

Cell behaviors are analyzed for C-rate and thermal effects, respectively. The rate effect is examined by comparing the cell resistance at an infinitely small discharge rate with that at higher discharge rate assuming no temperature rise, i.e. under the isothermal condition which can be simulated by setting an infinitely large heat transfer coefficient between the cell and the ambient. The dependence of resistance on discharge rate would vanish if the cell were ohmically controlled. The thermal effect is delineated by comparing the cell resistance at the isothermal condition with that at a convective heat transfer condition. The ambient temperatures of 25°C and −20°C are chosen to represent room-temperature and subzero performance, respectively.

Low rate resistances.— C/1000 rate (2.2 mA) is used to simulate low rate discharge. At such low rate, electrolyte concentration polarizations are negligible. The electrolyte becomes an ohmic resistor whose resistance is determined by ionic conductivityκ and current transport length l:

$$R_e = c\frac{l}{\kappa\varepsilon^p} \qquad [16]$$

Regarding interfacial kinetics, low discharge rate implies small overpotential on particle interface, which allows using linear form of Butler-Volmer equation for interfacial kinetics with good approximation. Accordingly, the equivalent resistance for charge transfer is obtained:

$$R_k = \frac{1}{La}\frac{RT}{i_0(\alpha_a + \alpha_c)F} \qquad [17]$$

where L is the electrode thickness, a is the specific surface area, i_0 is the exchange current density, α_a and α_c are reaction transfer coefficient, R is the universal gas constant, T is the temperature, and F is the Faraday constant.

For solid-state diffusion inside active material particles, with the help of diffusion length concept,[50] the lithiation/delithiation rate on the particle surface is expressed as:

$$-D_s\frac{c_{si}-\bar{c}_s}{l_D}=\frac{I}{aA_eL} \quad [18]$$

where D_s is the solid-state diffusivity, l_D is the diffusion length equal to one fifth of particle radius r_p at steady state,[50] specific surface area a can be expressed as $3\varepsilon/r_p$. c_{si} and $\bar{c}$ are interfacial Li-ion concentration and average Li-ion concentration in the particles. At low discharge rate, the deviation of c_{si} to $\bar{c}_s$ is small. It is therefore safe to use:

$$U(c_{si})=U(\bar{c}_s)+\frac{dU}{dc_s}(c_{si}-\bar{c}_s) \quad [19]$$

Combining equation 18, 19 gives cell resistance due to concentration polarization inside particles:

$$R_p=\frac{|U(c_{si})-U(\bar{c}_s)|}{I}=\frac{dU}{dc_s}\frac{r_p^2}{15D\varepsilon L} \quad [20]$$

At 25°C, cell resistances as a function of SOC during low rate discharge are shown in Figure 6a. As expected, the electrolyte acts as a resistor. Its resistance remains constant throughout discharge because of negligible electrolyte concentration polarization. The anode possesses higher electrolyte resistance than the cathode, due to its lower porosity (0.26 vs. 0.28) and larger thickness (81 μm vs. 77 μm). The much larger porosity (0.46) and smaller thickness (20 μm) of the separator gives rise to lower electrolyte resistance. The combination of electrolyte resistance from anode, cathode and separator, as well as the contact resistance constitutes the bulk resistance of the cell, which is 28Ω cm^2 according to the model prediction. The bulk resistance dominates at room temperature. The kinetic resistance, mainly from the cathode, is low and varies with SOC due to the dependence of exchange current density on SOC. The kinetic resistance reaches maximum at discharged state. The above analysis on bulk and kinetic resistance coincides with Zhang's EIS study[13] on 18650 cells at 20°C.

At −20°C resistances display different trends as shown in Figure 6b. Kinetic resistances are more than an order of magnitude higher than room temperature and dominate all resistances. This is a result of the large kinetic activation energy, which is 68kJ/mol at the graphite anode and ∼50kJ/mol at the NCM cathode according to the recent study of Jow et al.[16] These two values are also used in the present model. The activation energy for charge transfer kinetics is much higher than those characteristic of other electrochemical and transport processes (∼30 kJ/mol for solid-state diffusion and 20 kJ/mol for electrolyte properties). In contrast to low-rate discharge at room temperature where anode kinetics are much faster than that of the cathode, at −20°C the kinetics of the graphite anode and NCM cathode reach a similar level because of the higher activation energy of graphite. At even lower temperature, anode kinetics would be rate-limiting. These analytical results of the charge-transfer resistance are in a good agreement with Tafel polarization measurements by Smart et al.[8] across a wide range of temperatures, as well as Zhang's EIS study[13] on 18650 cells at −20°C. From 25°C to −20°C, the electrolyte resistances experience seven times increases, from 22Ω cm^2 to 155Ω cm^2. They are fairly constant throughout discharge, except for a little fluctuation inside the anode, which is due to the non-uniform reaction there. The reaction front generated at the anode-separator interface moves toward the anode current collector, thereby extending the ionic current path. It seems that 1/1000 C discharge rate is insufficient to eliminate all non-uniformities at −20°C.

Additionally, our model predicts the resistance pertinent to the active material particles, as described in equation 20. This resistance is the combined effect of solid-phase diffusion and the variation of OCP with Li^+ concentration. In the entire SOC range, the anode particle resistance shows two peaks, which are closely related to the three plateaus (85 mV, 120 mV and 210 mV) in graphite OCP.[51] dU/dc_s values are fairly low in plateau regions, but become very large in the transition regions between two adjacent plateaus. At the same time, the uniform utilizations of graphite particles are expected at low discharge rates. The OCP influences are therefore superimposed by particles at different electrode locations, allowing the averaged graphite particle resistance to exhibit three troughs and two peaks. In the same way, the much higher starting particle resistance of NCM cathode is due to its large dU/dc_s compared with the graphite anode at the same cell SOC, in spite of smaller particle radius and two times larger solid-state diffusivity. These ups and downs in particle resistance are induced by thermodynamic OCP, and therefore are independent of temperature. This is why similar profiles of particle resistances are observed at both 25°C and −20°C, though with different magnitudes because of different solid state diffusivity at different temperatures. Both anode and cathode particle resistances increase rapidly at the end of discharge, due to the sharp change of voltage in graphite and NCM OCP curves at a discharged state. That of the anode increases more rapidly, implying anode-limited cell capacity.

The above simple analysis of low-rate resistances does not minimize its importance in description of the influence of thermodynamic and kinetic material properties on cell performance. The low discharge rate condition is a good approximation of equilibrium state, where large concentration polarizations and strong non-uniformities do not exist. Non-linear behaviors are simplified by linear approximation. Experimental analyzes, such as EIS, DC polarization and CV, are all performed close to cell's equilibrium state. It is possible to compare model prediction with electrochemical analysis data at/near this state.

High rate resistances.— During high-rate discharge, the large concentration polarization combined with sluggish kinetics results in strong non-linear and non-ohmic behaviors. Cell resistances during 4.6 C discharge at 25°C are shown in Figure 6c. A comparison with Figure 6a shows 40% reduction of discharge capacity due to large increase of electrolyte resistance and particle resistance in the anode. Herein $\Delta U/\Delta c_s$ should be used in equation 20 instead of dU/dc_s at high rate discharge because of a large concentration polarization. In addition, the non-uniform active material utilization distribution implies a large variation of $\Delta U/\Delta c_s$ for particles at different locations within an electrode. Whenever an average is taken here, the influence of OCP curve on particle resistance diminishes. As seen in Figure 6c, the anode particle resistance varies monotonically. Peaks and troughs that are shown at low-rate discharge are no longer displayed here, due to the dominant effect of solid phase diffusivity varying with SOC. The low value of dU/dc_s in the graphite plateau regions does not help to reduce the particle resistance during high-rate discharge. Instead, larger particle radius and smaller solid state diffusivity of graphite makes the anode solid diffusion limited. The cell capacity is actually determined by anode solid-state diffusion. As seen in Figure 6c, it is the anode solid particle resistance that has the most rapid increase before cutoff voltage is reached.

The electrolyte does not behave like a resistor during high-rate discharge. The electrolyte resistance in both the anode and cathode keeps increasing as discharge continues. The anode side increase is more marked. Compared with low rate discharge, the lower starting value of electrolyte resistance is attributed to shorter ionic current transport path because most of the reaction current is initially generated at locations close to the separator. To better explain the resistance increase, relevant electrolyte-parameter distributions along the cell thickness direction x at 2.5 V (just before cutoff) are shown in Figure 7. The voltage loss in the electrolyte is reflected by the decrease of electrolyte potential ϕ_e along x direction. The anode ϕ_e produces the largest potential drop, followed by cathode ϕ_e. The solution potential gradient can be expressed as:

$$-\nabla\phi_e=\frac{i_e}{\kappa}+\frac{\kappa_D}{\kappa}\nabla\ln c_e \quad [21]$$

which states that the electrolyte potential drop arises from two sources: ohmic loss and concentration overpotential. For ohmic loss, as observed in Figure 7, the ionic conductivity exhibits low values in both anode and cathode, since Li^+ ions accumulate in the anode electrolyte

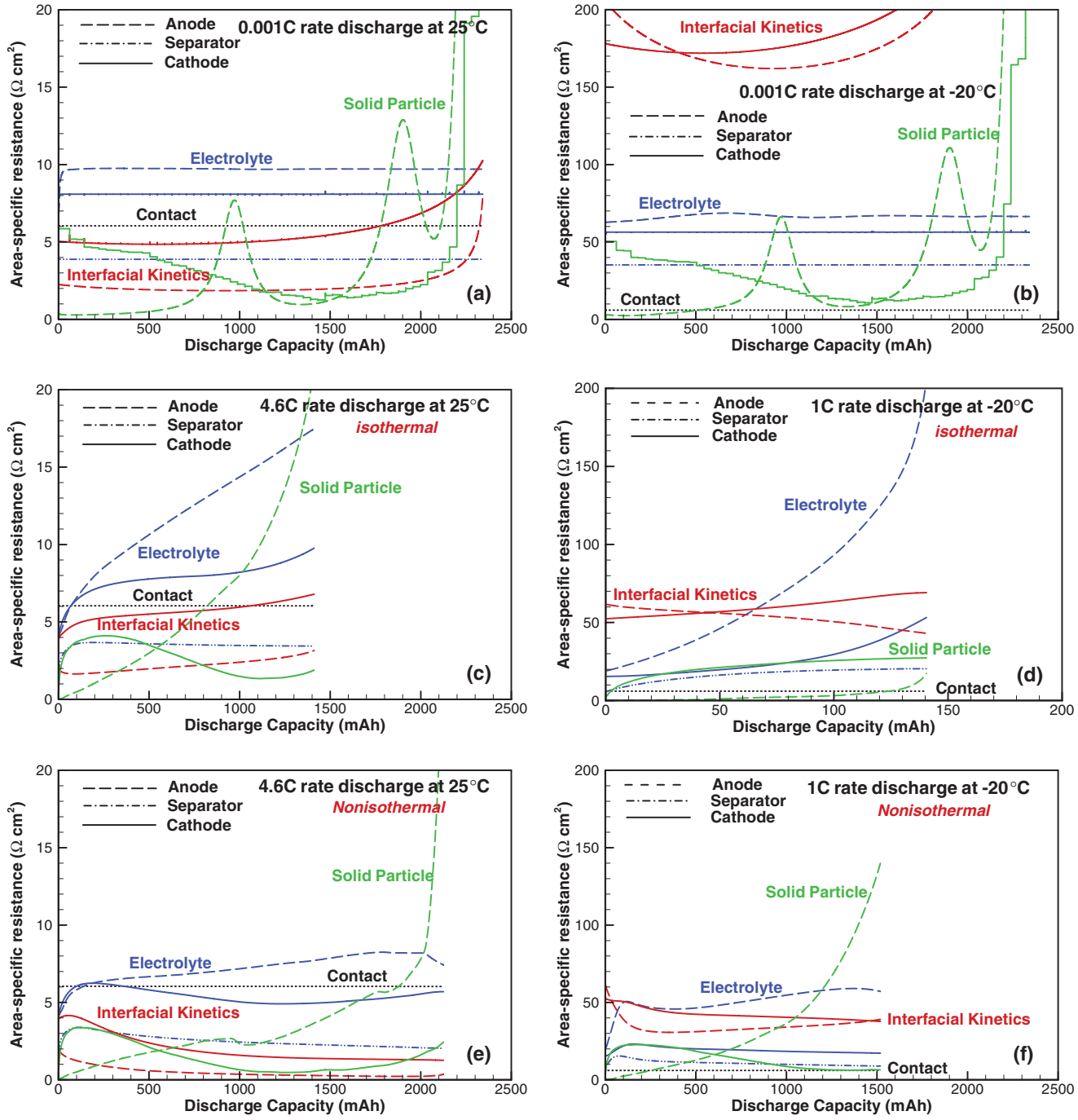

Figure 6. Cell resistance analysis at 25°C and −20°C.

(deintercalation from graphite particles) and are consumed in the cathode electrolyte (intercalation to NCM particles), both of which result in departures from the optimal concentration where maximum ionic conductivity is reached. In addition to the decreased ionic conductivity, concentration overpotential due to relatively large diffusional ionic conductivity in the anode aggravates the potential loss there. This diffusional ionic current is going in the reverse direction, thus larger electrolyte potential gradient is needed in the anode to balance this reverse current. The large diffusional ionic current is caused by the increased thermodynamic factor $(1 - t^+)(1 + d \ln f_\pm / d \ln c_e)$ that contributes to higher diffusional ionic conductivity. $d \ln f_\pm / d \ln c_e$ is an indication of short-range ion-solvent interactions, which can be ignored in dilute solutions, but may become dominant in high concentrated (>2.5mol/L) solutions.[52] As is observed in Figure 7, the electrolyte concentration c_e at the anode current collector reaches 3.6mol/L or three times the optimal level. This high concentration, on one hand, is due to the large Li-ion accumulation rate generated by high-rate discharge. On the other hand, it leads to the decreased salt diffusivity, which in turn increases the concentration gradient. This positive feedback between the salt diffusivity and electrolyte concentration induces an instability that might lead to cell shutdown if a threshold concentration is exceeded.

At −20°C, 1 C rate is used to study high rate resistances at subzero temperatures. During isothermal discharge, the cell voltage decreases quickly and reaches cutoff voltage at 140 mAh, which is only 6% of the room temperature capacity. The capacity loss is due to the large

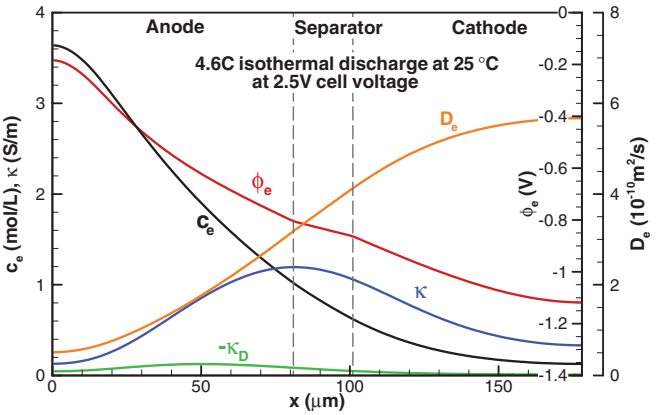

Figure 7. Electrolyte parameter distributions at the cutoff voltage of 4.6 C discharge at 25°C.

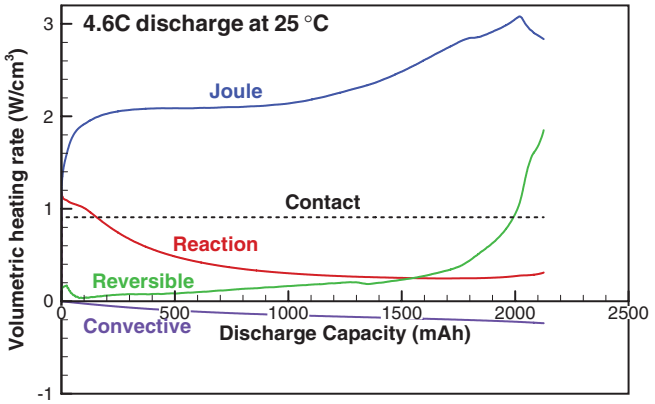

Figure 9. Heat generation during 4.6 C rate discharge starting from 25°C.

electrolyte resistance increase in the anode as shown in Figure 6d. To understand this, electrolyte parameter distributions at cell's cutoff voltage (2.5 V) are plotted in Figure 8. A steep drop in the electrolyte potential (∼0.9 V) occurs in the anode region close to the separator. The potential drop partially arises from the sharp decrease of ionic conductivity (by an order of magnitude), due to the elevated local concentration. Based on electrolyte property data from experiments,[52] at −20°C temperature, the electrolyte ionic conductivity is lowered significantly over a threshold concentration (3 mol/L). Careful examination of the concentration profile reveals that the electrolyte concentration exceeds 3 mol/L in the region where electrolyte potential drops significantly. On the other hand, part of the potential loss is contributed by concentration overpotential, due to the large value of κ_D/κ in concentrated solution, according to equation 21.

The electrolyte concentration drops rapidly in the cathode. At the cathode current collector interface, the electrolyte concentration reduces to depletion level (0.002 mol/L), which induces a large concentration gradient in the cathode, implying possible large concentration overpotential. However, κ_D/κ is small in this dilute solution. Thus potential loss from concentration polarization is limited. The ionic conductivity is also very low in dilute solutions, as seen in Figure 8. The ionic conductivity at cathode current collector reduces to the same level as it is in the anode. However, the total ionic current is small near current collector. The relevant ohmic potential drop is thus not that large as it is in the anode.

It is interesting to note a different kinetic resistance (around 60Ω cm^2) during 1 C discharge compared to the resistance (180Ω cm^2) during low (C/1000) rate discharge at −20°C, although the exchange current density remains the same without temperature change. Indeed,

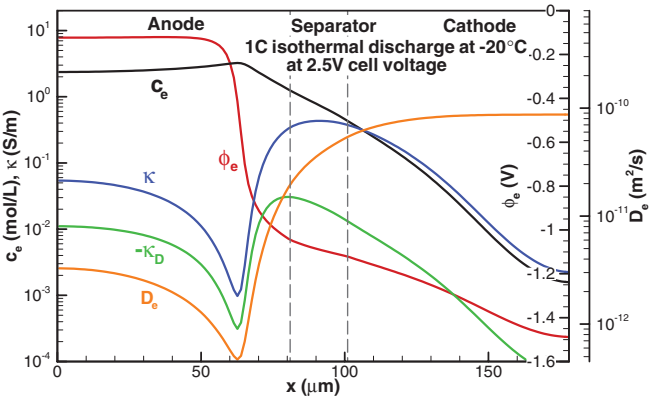

Figure 8. Electrolyte parameter distributions at the cutoff voltage of 1 C discharge at −20°C.

the charge transfer kinetics for 1 C rate discharge falls in the Tafel region, where the reaction current increases exponentially with overpotential, leading to lower kinetic resistance than that in linear region. Experimental investigations using EIS[11,13,14,27] and dc polarizations[3,27] are all performed using very small current as perturbations, where linear kinetics are studied. However, at higher rates, the Tafel kinetics is in control. Thus, caution should be exercised in interpreting these experimental results for cell operation at high rates.

Electrochemical-thermal coupling.— The above analysis shows large cell resistances when operating at high rates or low temperatures. It follows that heat generation from these resistances is significant and non-negligible, potentially leading to substantial cell temperature rise under practical heat-transfer conditions. The strong dependence of thermodynamic, kinetic and transport properties on temperature, on the other hand, provides feedback to cell performance due to temperature rise. In this way, electrochemical performance and thermal behaviors are intimately coupled.

Consider cells discharged at 4.6 C rate from 25°C with the thermal effect fully accounted for. Figure 6e shows cell resistance evolutions at this condition. Comparing with the isothermal condition (Figure 6c), the increase of electrolyte resistance and particle resistance slows down after ∼200 mAh discharge capacity with 10°C temperature rise seen from Figure 2. The anode electrolyte resistance still increases during discharge, but much slower, as a result of cell warmup. The charge-transfer kinetic resistance keeps decreasing with temperature rise due to its high activation energy. The anode particle resistance also decreases and its profile exhibit two small ups and downs, which are reflections of thermodynamic OCP characteristics, suggesting more uniform active material utilization and low solid-state concentration polarization. Overall, the electrolyte resistance is dominating at room temperature, high-rate discharge with electrochemical-thermal coupling fully considered. The contact resistance comes next. The resistance trend is quite similar to that at extremely low rate discharge shown in Figure 6a, where the electrolyte and contact resistance are dominating and staying at a constant level. From this point of view, with thermal effect considered at room temperature, the cell behaves like an ohmic resistor because cell resistances are roughly independent of discharge rates.

Heat generation rates from various sources are plotted against discharge capacity in Figure 9. The definitions of these heat terms can be found in equation 12. In according with resistance characteristics, joule heating and contact resistance heating are the primary heat generation sources. The reversible entropic heat is negligible during the first 1500 mAh discharge capacity, but increases significantly when approaching the end of discharge, owing to the large value of dU/dT of graphite at fully discharged state. The convective heat is the heat dissipated by convective air cooling. Most of the heat generated is used to heat up the cell due to small heat dissipation rate.

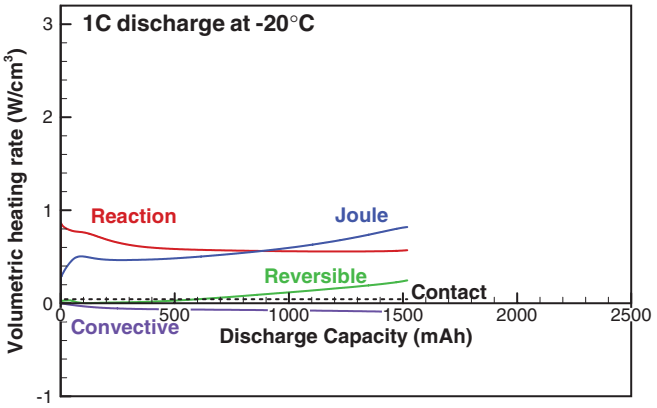

Figure 10. Heat generation during 1 C rate discharge starting from −20°C.

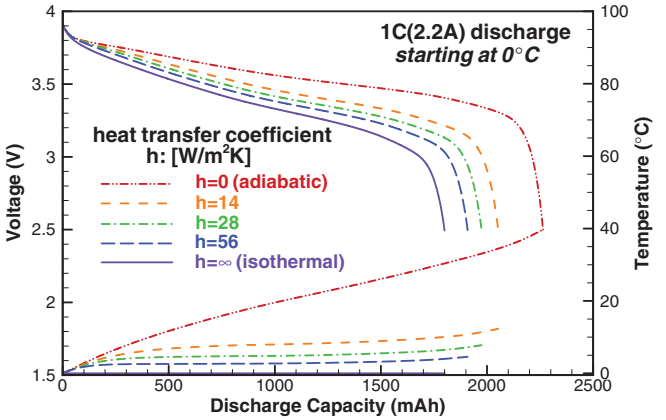

Figure 11. Cell performance at various cooling conditions (1 C discharge starting from 0°C).

At −20°C and 1 C discharge, various cell resistances and heat sources are plotted in Figure 6f and Figure 10, respectively, with thermal effect. Benefiting from cell self-heating, the discharge capacity increased from 140 mAh at the isothermal condition to 1500 mAh. The capacity gain is mainly attributed to the suppression of anode electrolyte resistance due to higher ionic conductivity and salt diffusivity resulting from temperature rise. Despite large activation energy of exchange current density, the kinetic resistances do not show significant decrease with temperature increase, possibly because of the transition from Tafel region to linear kinetics. The solid particle resistance in the anode, however, increases continuously and induces large potential drop after 1000 mAh discharge capacity, in spite of more than 10°C rise of cell temperature. With the transition from isothermal condition to convective heat transfer condition, the cell limiting step switches from the anode electrolyte to the anode solid-state diffusion.

Heat generation in discharge from −20°C (Figure 10) behaves differently from the room temperature case. Instead of the dominance of ohmic heating throughout the discharge process at room temperature, irreversible reaction heat contributes to most of heat generation for the first half for discharge starting at −20°C, though joule heating takes over in the remainder of discharge. The contact heating and reversible heating become negligible since they are small compared to other resistances that increase drastically with lowering temperature.

At subzero temperatures the dependence of cell resistance on discharge rates is strong due to non-linear kinetics, large concentration polarizations in solid particles and electrolyte, in spite of cell self-heating. Figure 4 provides a visual look at the non-ohmic behavior starting at −10°C. Unlike room temperature case, the discharge curves at various rates are not similar.

Nonisothermal Ragone plot.— Cell discharge performance at other heat-transfer conditions is studied to explore the performance sensitivity to thermal conditions. Figure 11 and Figure 12 display cell 1 C rate discharge performance at 0°C and −20°C, respectively. Five heat transfer conditions are simulated at each temperature, including two extreme cases: adiabatic (i.e. h = 0) and isothermal (i.e. h→∞). At −20°C, cell performance is highly sensitive to heat transfer coefficients. The cell capacity increaes from 140 to 2250 mAh when the thermal condition is switched from isothermal to adiabatic. At 0°C, however, the difference becomes smaller. The temperature increase from 0°C is also much smaller than it is from −20°C due to smaller resistance. The low isothermal performance at −20°C implies large cell resistance, and consequently stronger electrochemical-thermal interactions and larger performance boost, which is most significant at adiabatic condition. For instance, staring at −20°C with adiabatic condition, the cell is able to discharge most of its nominal capacity at room temperature. For starting temperature higher than 0°C, 1 C rate is not large enough to induce noticeable performance differences at various cooling conditions because of reduced cell resistances.

The above investigation shows strong dependence of cell performance on thermal boundary condition at subzero temperatures. Hence, it is necessary to prescribe cell thermal parameters when evaluating its performance at subzero temperature or during high-rate operation. The Ragone plot, defined as the specific energy vs. the specific power, is widely used for comparison of energy storage devices in terms of energy and power capabilities. However, when it is used for thermally coupled batteries such as Li-ion cells, important cell self-heating effect is not included. In this study, we introduce a nonisothermal Ragone plot to include thermal effects under normal heat-transfer conditions. We shall show that this nonisothermal plot is more relevant for Li-ion cells designed to operate at subzero temperatures.

To generate the nonisothermal Ragone plot, the present cell is discharged under constant power over a vast range of power values until a cutoff voltage of 2.5 V. The discharge energy is then calculated by time integration of the power. To calculate specific energy and specific power, the mass of the whole cell (44g) is used, including the jelly roll as well as can and other packaging masses. Model calculations are performed at four different temperatures: 25°C, 0°C, −10°C and −20°C. At each temperature, an isothermal curve and a nonisothermal curve under the experimental cooling conditions are plotted, as shown in Figure 13. As expected, with the increase of the specific power, the specific energy decreases for all cases. At the isothermal condition, the decrease in specific energy becomes prominent from 3 C rate at 25°C, 1 C rate at −10°C and even lower rate at −20°C. With the self-heating effect included, the decline points of the specific energy are largely deferred. The nonisothermal Ragone plot suggests that starting from −20°C or higher temperatures, the cell suffers no significant energy

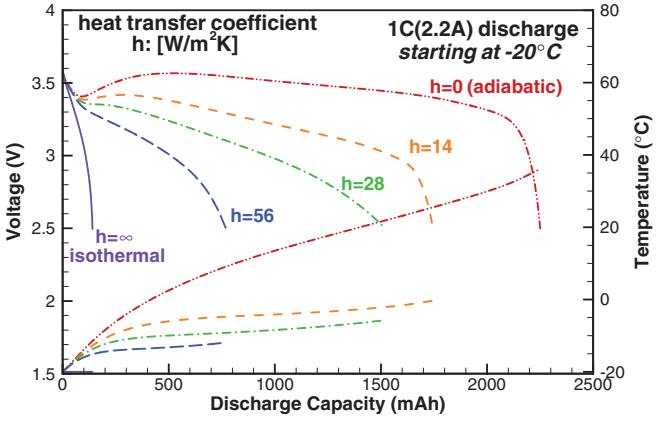

Figure 12. Cell performance at various cooling conditions (1 C discharge starting from −20°C).

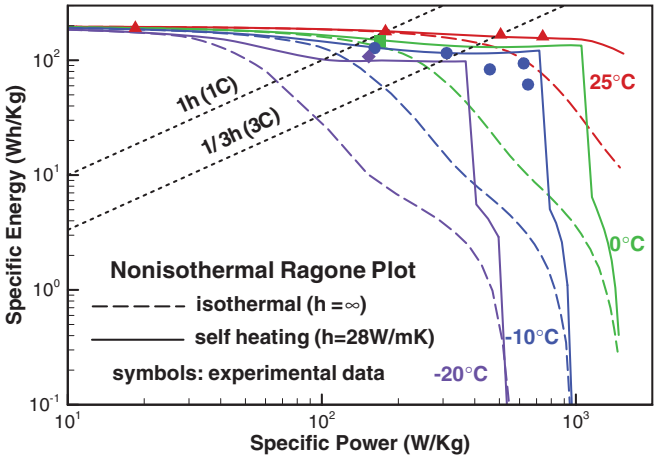

Figure 13. Nonisothermal Ragone Plot.

loss provided that the cell is operated at 3 C rate and lower. This is a new insight for Li-ion cell operation at low temperatures. A salient feature in the nonisothermal Ragone curve is a "power cliff", over which a steep reduction in the specific energy is triggered. The cliff is a result of competitions between the voltage loss induced by high power and the performance gain due to temperature increase from cell self-heating. The benefit from the thermal effect is small at low power where the self-heating effect is negligible. It is also irrelevant at very high power where fast voltage drop does not provide enough time to induce meaningful temperature rise. Only at moderate to high power could the electrochemical-thermal coupling provide significant boost on cell energy-power capability.

Cell Optimization for Subzero Operation

The significantly reduced energy-power capability of Li-ion cells at subzero temperatures has spurred research and development to improve cell performance in a variety of ways, including synthesizing novel electrolytes and using nanoparticles and surface coating for active materials. However, there is a lack of basic understanding of how much performance boost may be expected from these measures. The present study has found that the limiting mechanism at subzero temperatures depends on cell operation rates as well as thermal parameters including heat transfer to the ambient. Conventional electrochemical techniques are useful tools to characterize cell performance at low rates or near equilibrium state, but may not be able to accurately represent cell operation at higher rates, where capture and precise characterization of strong non-ohmic behaviors and thermal effects are beyond the scope of these tools. In this section, with the help of the experimentally validated ECT model, we attempt to optimize low-temperature cell performance.

Cell performance improvement at subzero temperatures can be achieved chiefly in three ways: developing new battery materials with desired properties, optimizing cell design and fabrication parameters, and preheating cells with innovative heating strategies (i.e. system approaches). This section is focused on the first two methods, while effective heating strategies will be pursued in a separate publication. The optimization will be conducted by modeling the influence of a variety of design parameters and material properties on cell discharge behavior separately. For each parameter or property investigation, the cell is subjected to discharge starting from −20°C with 1 C rate using two heat transfer settings (isothermal and self-heating), respectively. The isothermal condition represents cells with infinitely large cooling rate, which effectively eliminates any temperature rise in the cell. The self-heating case describes a realistic heat-transfer condition where significant temperature rise accompanies cell operation.

Design parameters.— For cell design optimization, we study influences of the electrode thickness, electrode porosity, electrolyte concentration, and particle size of active materials. The present 18650 test cells are used as the baseline. For each parameter study, only one parameter is varied around the baseline value while all other parameters remain at the baseline. Cell voltage and temperature curves as a function of discharge capacity are displayed in Figure 14.

Figure 14a, 14b demonstrates optimization results on the electrode thickness. The anode thickness of 60 μm, 70 μm, 81 μm, 90 μm is used and the cathode thickness is adjusted accordingly to maintain the (negative to positive) NP ratio of 1.15. The thickness changes are realized by adjusting active material loading amount without changing electrode porosities. Thinner electrodes demonstrate improved low-temperature performance at both isothermal and self-heating conditions. Physically, thinner electrodes imply shorter ionic current transport path and smaller current density due to enlarged electrode coating area, both of which are effective ways to reduce the voltage loss in the electrolyte. Indeed, significant improvement due to thinner electrodes is seen at the isothermal condition (Figure 14a). However, the capacity gain from the thinner electrode design at the self-heating condition (Figure 14b) is negligible because solid-state diffusion in graphite is the capacity-limiting step and is minimally affected by thinner electrodes. Finally, comparison of Figure 14a with Figure 14b clearly indicates that it is quite misleading to optimize cell design parameters based on isothermal electrochemical models for Li-ion cell operation at low temperatures.

Optimization of electrode porosities is shown in Figure 14c, 14d. The anode electrode porosity varies from 0.2 to 0.4 by changing active material loading amount, while electrode thicknesses are kept the same, i.e. electrodes of varying loadings are calendared to the same thickness. Large variations of cell performances are observed in Figure 14c. High porosity electrode leads to both increased voltage and capacity during isothermal discharge at −20°C. The performance gain comes from the reduced effective electrolyte conductivity and salt diffusivity, due to less torturous transport paths in porous electrodes with larger void space. For the self-heating condition (Figure 14d), however, the cell capacity begins to decrease when electrode porosity is higher than the baseline case. This happens because cell capacity is limited by solid-state diffusion in graphite for the self-heating case. The specific surface area (BET area divided by the electrode volume) for lithium intercalation is lowered when the void space volume increases, implying higher concentration polarization due to larger interfacial flux. In addition, the cell capacity decreases because of less active material loaded at higher porosity. The cell capacity is more sensitive to electrode porosity than electrode thickness (20% capacity loss if anode porosity increases from 0.26 to 0.4). This capacity loss outweighs the voltage gain from increased electrolyte conductivity and salt diffusivity. Again, the porosity optimization results differ sharply between the isothermal and self-heating cases.

The idea of changing electrolyte concentration is prompted from the dependence of electrolyte conductivity and salt diffusivity on solution concentrations. For isothermal discharge at −20°C, as analyzed in Figure 8, large electrolyte potential drop is induced by significantly reduced conductivity and diffusivity at the location where electrolyte concentration exceeds 3 mol/L. It is expected that using a dilute solution, the decrease of electrolyte conductivity and salt diffusivity may be avoided. The modeling result from Figure 14e, 14f does indicate slightly improved performance for concentration of 0.9 mol/L, for both the isothermal and self-heating cases. However, more decrease or increase in the solution concentration would lead to worse performance. For the 0.6 mol/L case, cell voltage keeps decreasing at the isothermal condition, and rebounds when self-heating is included. For the 1.7 mol/L case, the cell voltage fails to rebound at self-heating condition, where discharge capacity is substantially limited (<100 mAh). Overall, the optimized electrolyte concentration exists between 0.9 and 1.2 mol/L. A relatively lower value is preferred whenever the anode electrolyte resistance is limiting, and vice versa.

The last design optimization aims to increase cell capacity under the self-heating condition. Since solid-state diffusion in the anode is

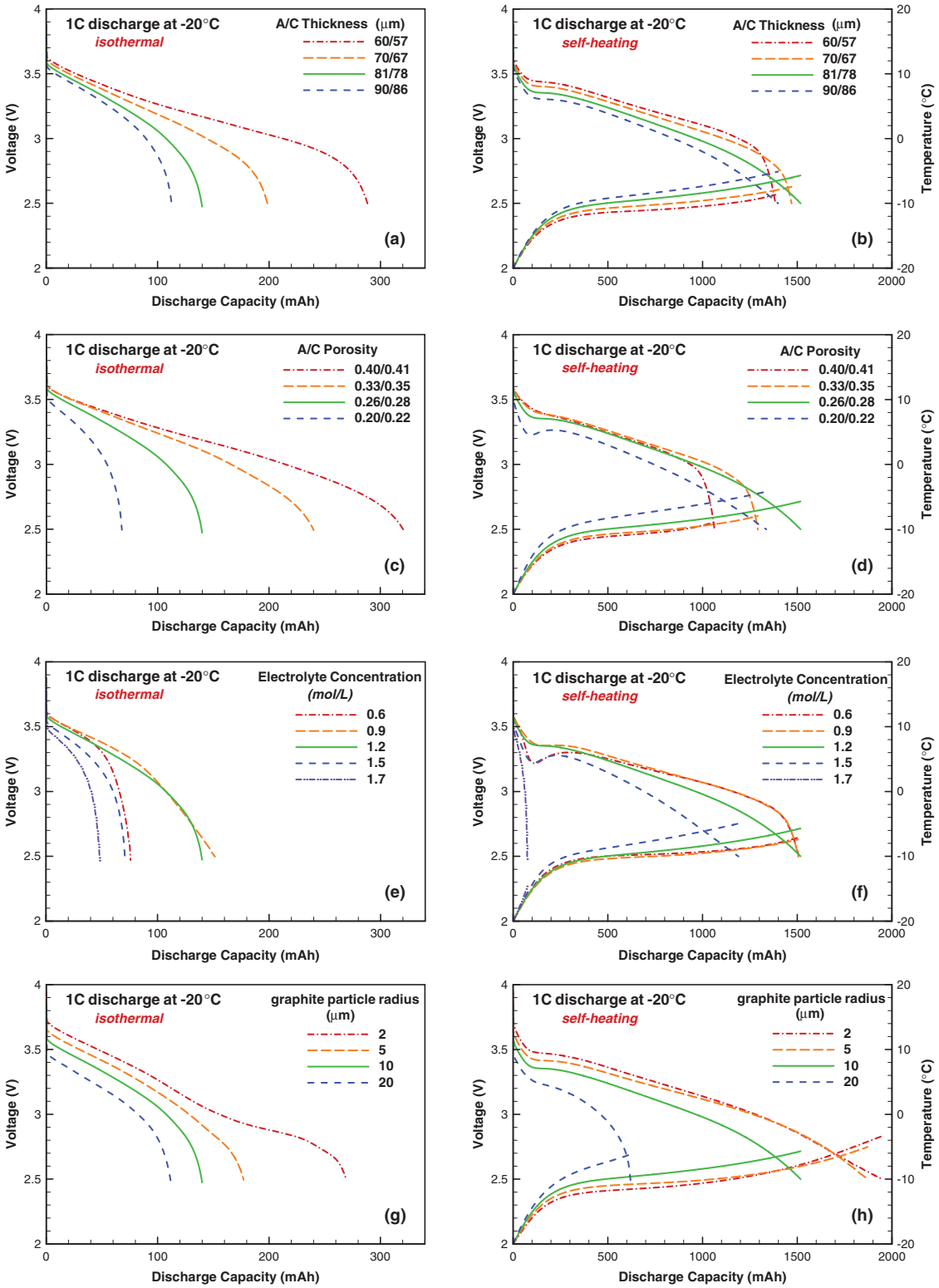

Figure 14. Optimization of cell design parameters.

the limiting step in this application, an effective way of relieving this limitation is to use smaller particles, thereby decreasing the diffusion length and increasing the BET area for reaction. As shown in Figure 14h, significant capacity gain (18% cell design capacity) has been achieved with the use of particle with half radius (5 μm). Further reduction in particle size does not lead to notable performance increase, implying that the cell with smaller graphite particles is no longer limited by anode solid-state diffusion. The capacity gain by decreasing the particle size is not appreciable at the isothermal condition, because the cell is limited by electrolyte resistance there.

To summarize, the two most notable findings from the cell design optimization for −20°C operation under realistic thermal boundary conditions are that: (1) reducing the graphite particle radius is very effective to enhance cell performance; and (2) increasing the electrolyte

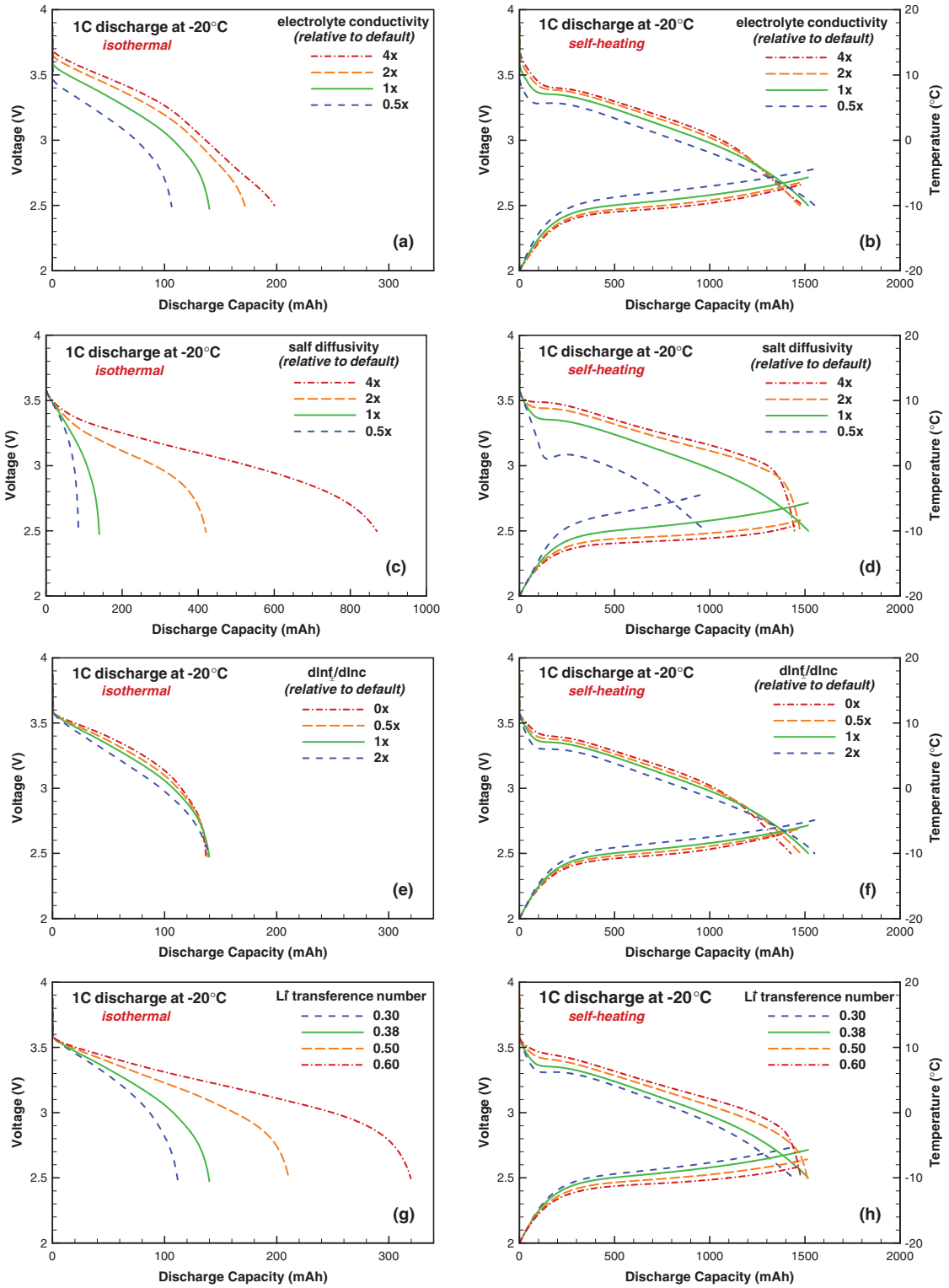

Figure 15. Optimization of electrolyte properties.

concentration beyond 1.2 M may substantially lower the cell discharge capacity.

Material properties.— Search for novel materials with optimal properties is of great interest to improve cell performance at low temperatures. Of all cell materials, active materials and electrolyte directly impact cell performance. The electrolyte properties include ionic conductivity, salt diffusivity, Li^+ transference number, etc. These properties can be modified by employing different salt and solvent, or adding co-solvents and additives in the electrolyte. For active materials, relevant properties include the exchange current density describing charge transfer kinetics and solid-state diffusivity for Li diffusion. Alteration of these properties can be practically achieved by doping, surface coating, or modifying synthesis methods or conditions.

Optimization results of electrolyte properties are summarized in Figure 15. The property data used for experimental validation serve

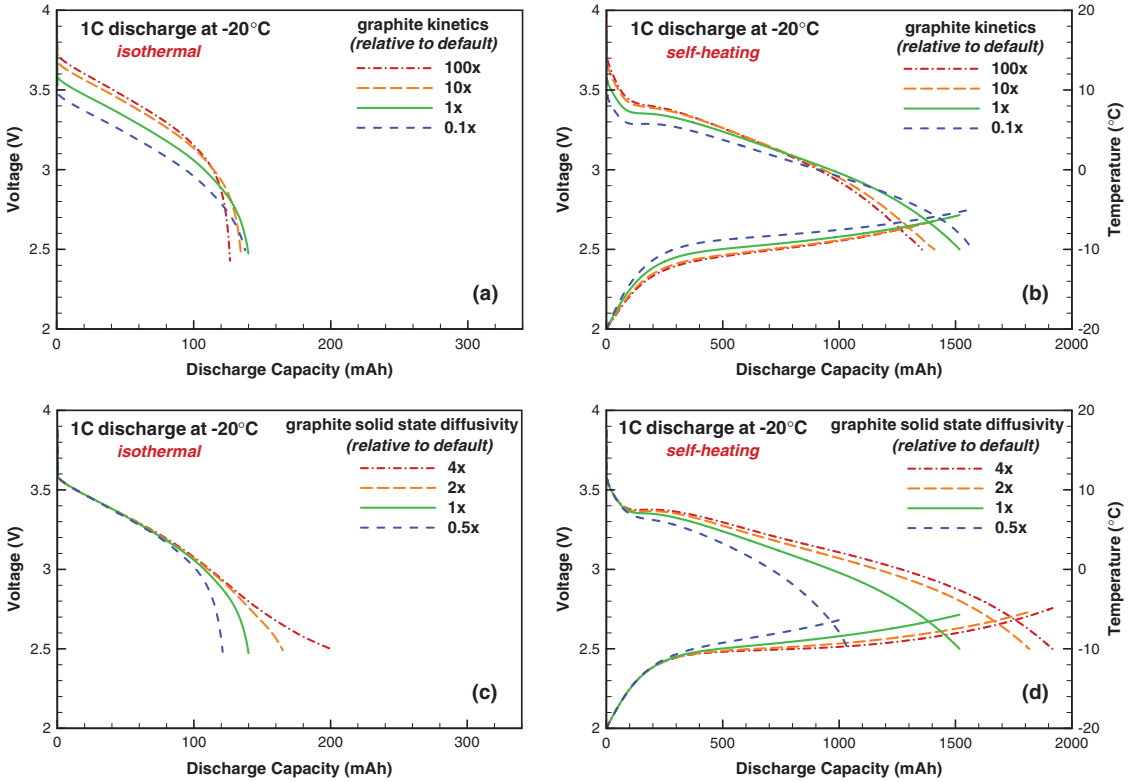

Figure 16. Optimization of active material properties.

as the baseline case, whose discharge curves are plotted as solid green lines. Three multipliers are applied to the baseline value for each parametric study without changing their dependences on concentration and temperature. For all optimization studies, cells are discharged at 1 C rate and starting from −20°C under the isothermal condition and self-heating condition, respectively.

As shown in Figure 15a, 15b, the electrolyte conductivity, although widely perceived as the most important property of electrolytes, does not show significant effect on cell discharge at the isothermal condition, and has even less effect under the self-heating condition. On the other hand, as shown in Figure 15c, with use of 4× baseline salt diffusivity, the cell discharge capacity at isothermal condition increases from 150 to 900 mAh. That is the largest increase found in the present study and thus, a huge step forward in optimization. It implies that the anode electrolyte resistance, which is the primary resistance for 1 C rate discharge at −20°C, is induced by the limited salt diffusion rate. Returning to Figure 8, although the ionic conductivity is apparently the reason for electrolyte potential drop, the low salt diffusivity is the underlying reason for local Li^+ accumulation and ultimately leads to much reduced conductivity locally. The elevation of salt diffusivity is far more beneficial than increasing the conductivity since the cell performance is more mass transport limited than ohmic resistance limited. At the self-heating condition, the salt diffusivity also exhibits great importance. As shown in Figure 15d, with half salt diffusivity used, the cell voltage keeps decreasing until 3 V cell voltage is reached. Without benefitting from 10°C cell temperature rise, or with larger cell cooling rate, the cell voltage may not be able to recover and the cell would shut down at a very low discharge capacity.

In the optimization study described above, the ionic conductivity and salt diffusivity are treated to vary independently. In reality, the two properties are not independent, but interconnected by the ion mobility. Their link is complex for concentrated solutions or in the presence of co-solvents and additives. At any rate the salt diffusivity merits full attention in evaluation of novel electrolytes for Li-ion cells, especially during low-temperature operation.

Additionally, we investigate effects of two other electrolyte properties: the salt activity $f_{\pm}$ and cation transference number t_+. The activity coefficient $f_{\pm}$, which is a representative of short-range ion-solvent interactions, increases rapidly with concentration in concentrated solutions. Accordingly, $d \ln f_{\pm}/d \ln c$, approaches zero in very dilute solutions but becomes non-negligible in concentrated solutions. As shown in Figure 15e, 15f, cell voltage displays little change even if ideal behaviors (i.e. the 0× case) are assumed. These results indicate small influences of salt activity, implying that the concentration overpotential is not that significant for 1 C discharge at −20°C. The cation transfer number determines the source or sink of the solution transport equations. There would be no solution concentration polarizations if unity cation transfer number were used. The influences of cation transfer number are shown in Figure 15g, 15h. At the isothermal condition, the cell capacity is doubled when cation transference number increases to 0.6. Since cell performance is solution phase diffusion limited at −20°C, the large value of cation transference number alleviates concentration polarization, leading to increased cell capacity. At the self-heating condition, the cell capacity changes little, but higher voltages are observed, because of decreased electrolyte resistance from less polarized concentration.

In addition to the electrolyte properties, optimization of active material properties is also conducted. Under the isothermal condition at −20°C, as shown in Figure 6d, interfacial kinetic resistance dominates during the first half of discharge. Under the self-heating condition, as shown in Figure 6f, large kinetic resistance is observed at the beginning of discharge while the anode particle resistance increases rapidly and becomes controlling during the rest of discharge. To reduce these major resistances, optimization of the exchange current density and solid-state Li diffusivity in graphite anode is performed, as shown in Figure 16. Since the charge transfer kinetics falls in the Tafel regime, to produce visible differences in cell voltage, the exchange current density is changed by orders of magnitude. It is seen that at the isothermal condition (Figure 16a), charge transfer kinetics impact on cell voltage is insignificant (∼100 mV when kinetics is 10 times faster); there is also little benefit to cell discharge capacity.

Under the self-heating condition (Figure 16b), the cell capacity even decreases by 7% because of less benefit from insufficient temperature rise owing to reduced kinetic resistance. Optimization of the graphite solid state diffusivity yields an entirely different scenario. As shown in Figure 16c, 16d, when the diffusivity is doubled, the cell is able to discharge 16% higher capacity at the isothermal condition and 20% higher capacity at the self-heating condition.

Conclusions

Li-ion cell operation at subzero temperatures has been studied experimentally and theoretically. An electrochemical-thermal coupled (ECT) model was validated against experimental data on a 2.2Ah 18650 cell over a wide range of C-rates and ambient temperatures, with generally good agreement. The experimentally validated ECT model was subsequently used to gain insight into and for optimization of Li-ion cells operated at low temperatures. The following conclusions are drawn:

(1) Cell behavior depends not only on the ambient temperature, but also on the operation rate and thermal conditions. At −20°C, charge transfer kinetics is the limiting factor in low-rate (C/1000) operation. For 1 C discharge under the isothermal condition, however, the anode electrolyte resistance becomes dominant, due to highly reduced ionic conductivity from large electrolyte concentration polarizations. When cell self-heating effect is included, the electrolyte concentration polarization is alleviated, making the resistance in anode solid particles a limit for both cell voltage and capacity.

(2) The ECT coupling becomes stronger with increasing C-rate and decreasing ambient temperature. The cell performance is more sensitive to the heat transfer condition at low temperatures, due to the enhanced self-heating from higher resistance and stronger temperature dependence of material properties in that temperature range. At −20°C, the change of heat transfer condition from isothermal to adiabatic leads to a huge increase in discharge capacity, e.g. from 140 to 2200 mAh.

(3) The non-isothermal Ragone plot is proposed for the first time for applications at high rates and/or low temperatures, where substantial performance enhancement can be realized by cell self-heating. The nonisothermal Ragone plot indicates no significant energy loss down to −20°C (ambient temperature) provided that the cell is operated at 3 C rate or lower.

(4) For operation at −20°C, decreasing the graphite particle radius is very effective to enhance cell performance, while increasing the electrolyte concentration beyond a critical level (1.2 M in the present study) may substantially lower the cell discharge capacity.

(5) For material property optimization for cell operation at −20°C, increasing salt diffusivity in electrolyte and solid-state Li diffusivity in graphite particles are most beneficial to improve cell discharge capacity.

Acknowledgments

Partial support of this work by DOE CAEBAT program and Korean Agency of Defense Development (ADD) is greatly acknowledged. We are also grateful to EC Power for offering numerical algorithms and materials database through its AutoLion software.

Appendix A: Mathematical Definitions of Various Cell Resistances

To analyze the contributions from various transport and kinetic processes, breakdown of the cell voltage drop relative to open circuit potential (OCP) is necessary. Considering non-uniform distributions in each electrode and the separator, for any physical quantity ξ, average is taken over the thickness to represent its level in an electrode or separator:

$$\bar{\xi} = \int_L \xi \, dl \qquad [A1]$$

where L is the thickness of an electrode or separator. Voltage losses due to electronic resistance in the two electrodes are:

$$\Delta V_s^A = V^A - \bar{\phi}_s^A \qquad \Delta V_s^C = \bar{\phi}_s^C - V^C \qquad [A2]$$

in which V^A and V^C are potentials at the anode-foil interface and the cathode-foil interface respectively. Voltage losses induced by ionic resistance and concentration overpotential in electrolyte are:

$$\Delta V_e^A = \bar{\phi}_e^A - \phi_e^{AS} \qquad \Delta V_e^S = \phi_e^{AS} - \phi_e^{SC} \qquad \Delta V_e^C = \phi_e^{SC} - \bar{\phi}_e^C \qquad [A3]$$

where ϕ_e^{AS} and ϕ_e^{SC} are electrolyte potential at the anode-separator interface and the cathode-separator interface respectively. The kinetic over-potentials in the anode and cathode are:

$$\Delta V_k^A = \bar{\phi}_s^A - \bar{\phi}_e^A - \bar{U}^A \qquad \Delta V_k^C = -\bar{\phi}_s^C + \bar{\phi}_e^C + \bar{U}^C \qquad [A4]$$

where $U = U(c_{s,i})$ is the equilibrium potential at the stoichiometry (or equivalently SOC) on the particle surface. Concentration polarization in active material particles leads to voltage derivations from open circuit at the same state of charge:

$$\Delta V_p^A = \bar{U}^A - E^A \qquad \Delta V_p^C = E^C - \bar{U}^C \qquad [A5]$$

where E^A and E^C are open circuit potentials of anode and cathode at the same SOC. In addition, there are contact resistances between foil and electrodes, foil and current collectors. Voltage losses due to all these contact resistances are:

$$\Delta V_c = (V^- - V^A) + (V^C - V^+) \qquad [A6]$$

where V^- and V^+ are potentials of negative current collector and positive current collector. Their difference is the cell voltage. Based on the above definitions, the sum of all voltage losses is exactly equal to the difference between cell OCP ($E^C - E^A$) and cell voltage ($V^+ - V^-$).

Appendix B: Material and Electrochemical Properties

The open circuit potentials (OCP) of graphite (Li_xC_6) and NCM ($Li_yNi_{1/3}Mn_{1/3}Co_{1/3}O_2$) are obtained from experimental measurements reported by Verbrugge et al.[53] and Yabuuchi et al.[54] respectively, and have been fitted to empirical equations:

$$U\,(\text{Graphite}) = 0.1493 + 0.8493e^{-61.79x} + 0.3824e^{-665.8x} - e^{39.42x-41.92} - 0.03131\arctan(25.59x - 4.099) - 0.009434\arctan(32.49x - 15.74) \quad (0 \le x \le 1) \qquad [B1]$$

$$U\,(\text{NCM}) = -10.72y^4 + 23.88y^3 - 16.77y^2 + 2.595y + 4.563 \quad (0.3 \le y \le 1) \qquad [B2]$$

The reversible heat of graphite and NCM as a function of stoichiometric are obtained from the entropy change reported by Reynier et al.[55] and Lu et al.[56] respectively. Instead of fitting these data into empirical relations, discrete data points with linear interpolation are used in the present study.

With regard to electrolyte properties, Valoen and Reimers[52] reported experimentally a full description of electrolyte properties (ionic conductivity, salt diffusivity, cation transference number and activity coefficient) with dependency on concentration and temperature in the solution of PC (10%), EC (27%) and DMC (63%) (by vol) with $LiPF_6$ salt. The empirical data fittings given by Valoen and Reimers have been used for ionic conductivity and activity coefficient. For salt diffusivity, we have developed new correlations at low temperatures due to the fact that the electrolyte used in the present study contains 20% EMC, 20% EC and 60% DMC, slightly different composition optimized for enhancing salt diffusivity at low temperatures. These new correlations are shown in Figure B1

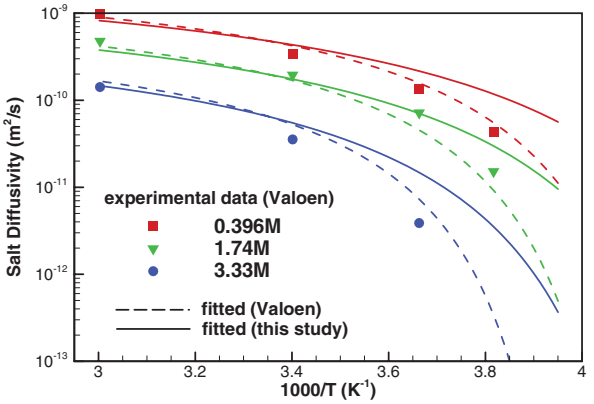

Figure B1. Salt diffusivity as a function of temperature.

along with the original experimental data of Valoen and Reimers and their fitted curves for comparison. Other active material properties are listed in Table II.

References

1. G. Nagasubramanian, *J. Appl. Electrochem.*, **31**, 99 (2001).
2. DOE, *Energy storage R&D annual progress report*, 81 (2011).
3. M. C. Smart, B. V. Ratnakumar, and S. Surampudi, *J. Electrochem. Soc.*, **146**, 486 (1999).
4. E. J. Plichta and W. K. Behl, *J. Power Sources*, **88**, 192 (2000).
5. H. C. Shiao, D. Chua, H. P. Lin, S. Slane, and M. Salomon, *J. Power Sources*, **87**, 167 (2000).
6. M. C. Smart, B. V. Ratnakumar, and S. Surampudi, *J. Electrochem. Soc.*, **149**, A361 (2002).
7. S. S. Zhang, K. Xu, J. L. Allen, and T. R. Jow, *J. Power Sources*, **110**, 216 (2002).
8. M. C. Smart, B. V. Ratnakumar, K. B. Chin, and L. D. Whitcanack, *J. Electrochem. Soc.*, **157**, A1361 (2010).
9. S. S. Zhang, K. Xu, and T. R. Jow, *Electrochem. Commun.*, **4**, 928 (2002).
10. S. S. Zhang, K. Xu, and T. R. Jow, *J. Power Sources*, **115**, 137 (2003).
11. S. S. Zhang, K. Xu, and T. R. Jow, *Electrochim. Acta*, **49**, 1057 (2004).
12. S. S. Zhang, K. Xu, and T. R. Jow, *J. Power Sources*, **159**, 702 (2006).
13. S. S. Zhang, K. Xu, and T. R. Jow, *J. Power Sources*, **160**, 1403 (2006).
14. A. N. Jansen, D. W. Dees, D. P. Abraham, K. Amine, and G. L. Henriksen, *J. Power Sources*, **174**, 373 (2007).
15. D. P. Abraham, J. R. Heaton, S. H. Kang, D. W. Dees, and A. N. Jansen, *J. Electrochem. Soc.*, **155**, A41 (2008).
16. T. R. Jow, M. B. Marx, and J. L. Allen, *J. Electrochem. Soc.*, **159**, A604 (2012).
17. C. K. Huang, J. S. Sakamoto, J. Wolfenstine, and S. Surampudi, *J. Electrochem. Soc.*, **147**, 2893 (2000).
18. H. P. Lin, D. Chua, M. Salomon, H. C. Shiao, M. Hendrickson, E. Plichta, and S. Slane, *Electrochem. Solid St*, **4**, A71 (2001).
19. S. S. Zhang, K. Xu, and T. R. Jow, *Electrochim. Acta*, **48**, 241 (2002).
20. C. S. Wang, A. J. Appleby, and F. E. Little, *J. Electrochem. Soc.*, **149**, A754 (2002).
21. J. Fan, *J. Power Sources*, **117**, 170 (2003).
22. J. Fan and S. Tan, *J. Electrochem. Soc.*, **153**, A1081 (2006).
23. M. Mancini, F. Nobili, S. Dsoke, F. D'Amico, R. Tossici, F. Croce, and R. Marassi, *J. Power Sources*, **190**, 141 (2009).
24. J. W. Yao, F. Wu, X. P. Qiu, N. Li, and Y. F. Su, *Electrochim. Acta*, **56**, 5587 (2011).
25. T. Yuan, X. Yu, R. Cai, Y. K. Zhou, and Z. P. Shao, *J. Power Sources*, **195**, 4997 (2010).
26. M. C. Smart, B. V. Ratnakumar, L. D. Whitcanack, K. B. Chin, S. Surampudi, H. Croft, D. Tice, and R. Staniewicz, *J. Power Sources*, **119**, 349 (2003).
27. M. C. Smart, J. F. Whitacre, B. V. Ratnakumar, and K. Amine, *J. Power Sources*, **168**, 501 (2007).
28. C. R. Sides and C. R. Martin, *Adv. Mater.*, **17**, 125 (2005).
29. J. L. Allen, T. R. Jow, and J. Wolfenstine, *J. Power Sources*, **159**, 1340 (2006).
30. M. Doyle, T. F. Fuller, and J. Newman, *J. Electrochem. Soc.*, **140**, 1526 (1993).
31. T. F. Fuller, M. Doyle, and J. Newman, *J. Electrochem. Soc.*, **141**, 1 (1994).
32. M. Doyle, J. Newman, A. S. Gozdz, C. N. Schmutz, and J. M. Tarascon, *J. Electrochem. Soc.*, **143**, 1890 (1996).
33. W. B. Gu and C. Y. Wang, *J. Electrochem. Soc.*, **147**, 2910 (2000).
34. L. Song and J. W. Evans, *J. Electrochem. Soc.*, **147**, 2086 (2000).
35. V. Srinivasan and C. Y. Wang, *J. Electrochem. Soc.*, **150**, A98 (2003).
36. K. Kumaresan, G. Sikha, and R. E. White, *J. Electrochem. Soc.*, **155**, A164 (2008).
37. R. E. Gerver and J. P. Meyers, *J. Electrochem. Soc.*, **158**, A835 (2011).
38. G. H. Kim, K. Smith, K. J. Lee, S. Santhanagopalan, and A. Pesaran, *J. Electrochem. Soc.*, **158**, A955 (2011).
39. G. Luo and C. Y. Wang, in *Lithium-ion Batteries : Advanced Materials and Technologies*, X. Yuan, H. Liu, and J. Zhang Editors, p. 303, CRC Press, Boca Raton (2012).
40. C. R. Pals and J. Newman, *J. Electrochem. Soc.*, **142**, 3274 (1995).
41. M. W. Verbrugge, *Aiche J.*, **41**, 1550 (1995).
42. G. G. Botte, B. A. Johnson, and R. E. White, *J. Electrochem. Soc.*, **146**, 914 (1999).
43. K. E. Thomas and J. Newman, *J. Electrochem. Soc.*, **150**, A176 (2003).
44. K. Smith and C. Y. Wang, *J. Power Sources*, **160**, 662 (2006).
45. W. F. Fang, O. J. Kwon, and C. Y. Wang, *Int. J. Energ. Res.*, **34**, 107 (2010).
46. T. M. Bandhauer, S. Garimella, and T. F. Fuller, *J. Electrochem. Soc.*, **158**, R1 (2011).
47. J. Y. Eom, L. Cao, and C. Y. Wang, *J. Power Sources*, submitted for publication (2013).
48. H. Maleki, S. Al Hallaj, J. R. Selman, R. B. Dinwiddie, and H. Wang, *J. Electrochem. Soc.*, **146**, 947 (1999).
49. E. P. Roth, Thermal Abuse Performance of MOLI, Panasonic and Sanyo 18650 Li-Ion Cells, in *Sandia Report SAND2004-6721*, Sandia National Laboratories (2005).
50. C. Y. Wang, W. B. Gu, and B. Y. Liaw, *J. Electrochem. Soc.*, **145**, 3407 (1998).
51. T. Ohzuku, Y. Iwakoshi, and K. Sawai, *J. Electrochem. Soc.*, **140**, 2490 (1993).
52. L. O. Valoen and J. N. Reimers, *J. Electrochem. Soc.*, **152**, A882 (2005).
53. M. W. Verbrugge and B. J. Koch, *J. Electrochem. Soc.*, **150**, A374 (2003).
54. N. Yabuuchi, Y. Makimura, and T. Ohzuku, *J. Electrochem. Soc.*, **154**, A314 (2007).
55. Y. F. Reynier, R. Yazami, and B. Fultz, *J. Electrochem. Soc.*, **151**, A422 (2004).
56. W. Lu, I. Belharouak, D. Vissers, and K. Amine, *J. Electrochem. Soc.*, **153**, A2147 (2006).
57. K. M. Shaju, G. V. S. Rao, and B. V. R. Chowdari, *J. Electrochem. Soc.*, **151**, A1324 (2004).
58. T. L. Kulova, A. M. Skundin, E. A. Nizhnikovskii, and A. V. Fesenko, *Russ. J. Electrochem.*, **42**, 259 (2006).